Article | Open Access

Energy Materials

Lu *et al. Energy Mater.* **2026**, *6*, 600115 **DOI:**10.20517/energymater.2026.162

Cross-linked coal-derived hard carbon with expanded interlayers and nanopores for high-plateau sodium storage

Cuiying Lu[1], Qianggong Dong[1], ChangXiang Guo[1,*], Zhen Wang[1], Yunqi Feng[1], Guangfeng Hu[1], Ting Su[1], Huarui Hao[1], Xingbin Yan[2], Bingjun Yang[3], Dong Cao[1,*]

Keywords:
Coal-derived hard carbon, sodium-ion batteries, cross-linking, expanded interlayers, plateau capacity

Citation: Lu, C.; Dong, Q.; Guo, C.; Wang, Z.; Feng, Y.; Hu, G.; Su, T.; Hao, H.; Yan, X.; Yang, B.; Cao, D. Cross-linked coal-derived hard carbon with expanded interlayers and nanopores for high-plateau sodium storage. *Energy Mater.* **2026**, *6*, 600115. https://dx.doi.org/10.20517/energymater.2026.162

Received: 9 Jun 2026
First Decision: 25 Jun 2026
Revised: 18 Aug 2026
Accepted: 2 Sep 2026
Published: 11 Sep 2026

Academic Editor: Yuping Wu
Copy Editor: Ping Zhang
Production Editor: Ping Zhang

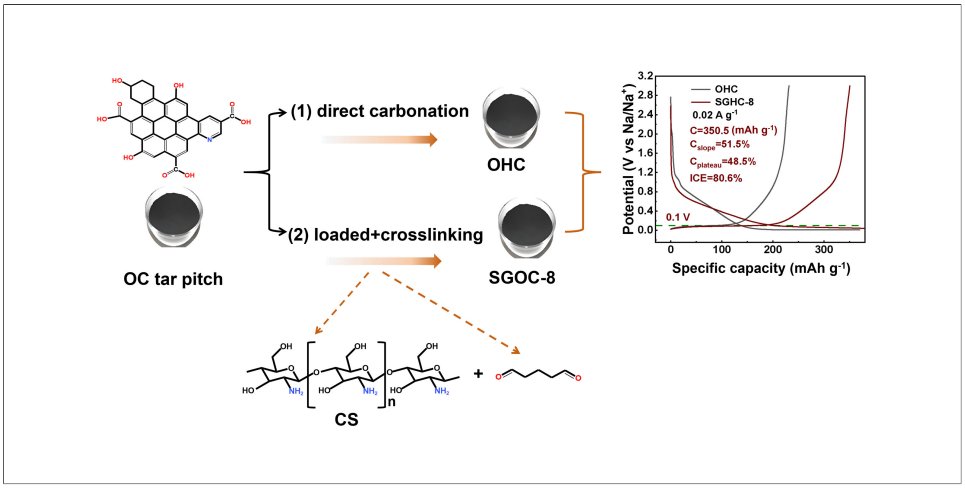

Abstract

Coal is a low-cost, carbon-rich feedstock for preparing hard carbon (HC) anodes, making coal-derived carbon attractive for sodium-ion battery applications. However, direct carbonization of coal usually involves softening, aromatization, and molecular rearrangement, which promote the ordered growth of graphitic microcrystals with limited interlayer spacing and insufficient nanopores, thereby restricting sodium-storage capacity. To address this issue, we introduce a chitosan/glutaraldehyde (CS/GA)-assisted molecular-network regulation strategy to tailor both the carbon framework and surface chemistry of coal-derived HC. CS is first immobilized on oxidized coal (OC) through hydrogen bonding and electrostatic interactions and then cross-linked with GA via a Schiff-base reaction, forming a molecular network that suppresses the ordered growth of graphitic microcrystals during carbonization. Meanwhile, chitosan serves as an

[1]Shaanxi Key Laboratory of Low Metamorphic Coal Clean Utilization, School of Chemistry and Chemical Engineering, Yulin University, Yulin 719000, Shaanxi, China.
[2]School of Materials Science and Engineering, Sun Yat-Sen University, Guangzhou 510275, Guangdong, China.
[3]Key Laboratory of Energy Conservation and Energy Storage Materials of Gansu Province, Research Center for Resource Chemistry and Energy Materials, State Key Laboratory of Solid Lubrication, Lanzhou Institute of Chemical Physics, Chinese Academy of Sciences, Lanzhou 730000, Gansu, China.

***Correspondence to:** Dr. ChangXiang Guo, Dr. Dong Cao, Shaanxi Key Laboratory of Low Metamorphic Coal Clean Utilization, School of Chemistry and Chemical Engineering, Yulin University, Yulin 719000, Shaanxi, China. E-mail: guo.cx168@yulinu.edu.cn; caodbit@yulinu.edu.cn

endogenous nitrogen source, enabling in situ nitrogen doping. The optimized SGHC-8 (CS/GA-cross-linked coal-derived HC) exhibits expanded interlayer spacing, increased defect density, and abundant nanopores, which contribute to enhanced sodium storage, especially in the low-voltage plateau region. As an anode for sodium-ion batteries, SGHC-8 delivers a reversible capacity of 350.5 mAh g^{-1}, an initial coulombic efficiency of 80.6%, and a plateau capacity contribution of 48.5%. Combined kinetic and structural evidence reveals that Na^+ storage in SGHC-8 proceeds through sequential adsorption, interlayer insertion, and nanopore filling. This work provides a feasible strategy for converting coal into high-performance HC anodes through cross-linking-induced microstructure regulation.

INTRODUCTION

Sodium-ion batteries (SIBs) are considered promising for grid-level energy storage owing to the natural abundance and wide distribution of sodium resources[1]. Despite rapid progress in cathode and electrolyte systems[2], anode materials still strongly determine the practical performance of SIBs[3,4]. An ideal anode should possess high reversible capacity, suitable working potential, good rate capability, and long-term structural stability[5,6]. Hard carbon (HC) remains the most practical anode option owing to its low operating voltage, tunable microstructure, good physicochemical stability, and cost-effective production[7,8].

Compared with biomass-derived precursors, coal offers advantages for scalable HC production due to its broad availability, low feedstock cost, high fixed-carbon content, and naturally formed aromatic skeleton[9,10]. These advantages make coal-derived HC promising for scalable SIB applications. However, the direct carbonization of coal, especially without deashing, is usually accompanied by softening, aromatization, and molecular rearrangement because of its complex molecular structure[11]. These processes promote the ordered growth of graphitic microcrystals, resulting in increased crystallinity, reduced interlayer spacing, and insufficient nanopore structure. Such structural features are unfavorable for Na^+ intercalation and low-voltage pore filling, leading to limited reversible capacity and poor plateau capacity in coal-derived HC anodes[12]. Therefore, the ordered growth of graphitic microcrystals and insufficient nanopore formation are the main structural bottlenecks limiting Na^+ storage behavior of coal-based HC.

Tuning the coal precursor before carbonization is an effective way to control the microstructure of coal-derived carbon and overcome these structural limitations for high-performance SIB anode materials. Various precursor-regulation strategies, including surface-chemistry manipulation[13], microcrystalline hybridization[14], precursor cross-linking[15], and pitch-assisted microcrystalline and defect regulation[16], have been employed to tailor the carbonization behavior and microstructure of coal-derived HC. Among these strategies, precursor cross-linking is particularly effective in strengthening the molecular framework, regulating pyrolysis behavior, restricting carbonization shrinkage, and promoting favorable disordered carbon structures and nanopores[15]. Nevertheless, because coal has a complex, heterogeneous molecular structure, a single treatment strategy is usually insufficient to simultaneously regulate microstructural features such as interlayer spacing, pore structure, and defect distribution. Therefore, an integrated molecular-level regulation strategy is required to construct coal-derived HC with favorable microstructures for high-plateau sodium storage.

Chitosan (CS), a nitrogen-rich biopolymer containing abundant amino and hydroxyl groups, is suitable for molecular-level modification of carbon precursors. Glutaraldehyde (GA) can bridge CS chains by reacting with their amino groups via Schiff-base chemistry, thereby generating a three-dimensional (3D) cross-linked network[17]. Such a network can stabilize the coal-derived precursor, restrict carbonization shrinkage, and suppress the ordered growth of graphitic microcrystals during carbonization. Meanwhile, heteroatom doping, especially nitrogen doping, has been widely used to improve the Na^+ storage behavior of HC by

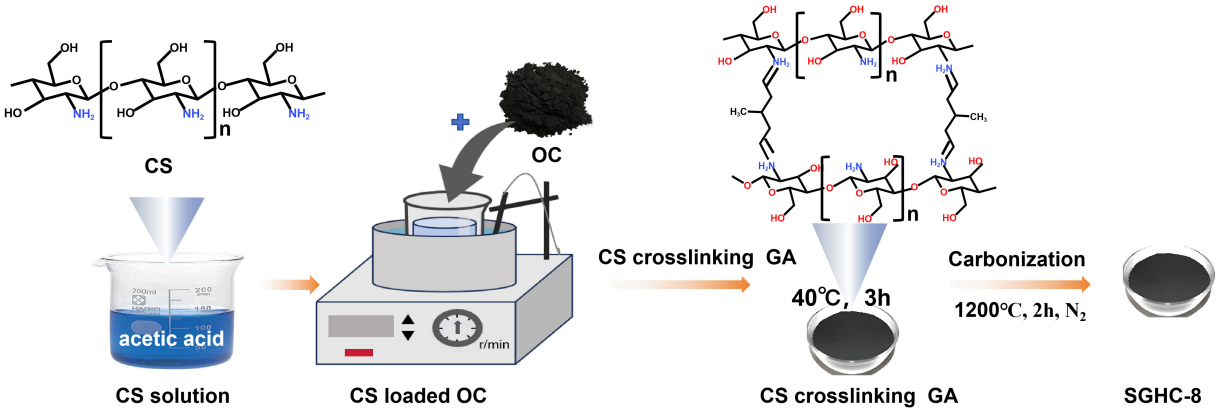

Figure 1. Schematic diagram showing the preparation of SGHC-8. CS: Chitosan; GA: glutaraldehyde; OC: oxidized coal.

modulating the local electronic structure, introducing defects, improving Na^+ affinity, and providing additional active sites[18-21]. Therefore, using CS as both a cross-linking component and an endogenous nitrogen source enables CS/GA cross-linking and in situ nitrogen doping. This integrated strategy is expected to regulate graphitic ordering, defect chemistry, and nanopore structure, thereby favoring high-plateau sodium storage[15,21,22].

Herein, cross-linked coal-derived HC with expanded interlayers and nanopores is developed for high-plateau sodium storage. CS is first immobilized on oxidized coal (OC) through hydrogen bonding and electrostatic interactions and then cross-linked with GA via a Schiff-base reaction, generating a molecular network that suppresses the ordered growth of graphitic microcrystals during carbonization. Meanwhile, CS serves as an endogenous nitrogen source, enabling in situ nitrogen doping and regulating the surface chemistry of the resulting HC. Benefiting from expanded interlayer distance, increased defect concentration, and abundant nanopores, the optimized SGHC-8 anode delivers a reversible capacity of 350.5 mAh g^{-1}, a high initial coulombic efficiency of 80.6%, as well as a plateau capacity contribution of 48.5%. Combined electrochemical and structural analyses reveal that sodium storage in SGHC-8 follows an adsorption-intercalation - pore-filling mechanism. This work provides a feasible molecular-network engineering strategy for converting coal into high-performance HC anodes for SIBs.

EXPERIMENTAL

Materials synthesis

Preparation of chitosan-loaded oxidized coal

OC refers to oxidized coal obtained from raw coal after the pre-oxidation treatment. Chitosan-loaded oxidized coal (SOC) was prepared by loading CS onto the OC surface. Typically, CS with a mass corresponding to 8 wt% of OC was fully dissolved in 100 mL of 1 wt% acetic acid solution at 500 rpm for 2 h at room temperature. Then, 1.0 g of OC was dispersed in the CS solution by stirring at 500 rpm for 3 h to facilitate CS adsorption. After the pH was adjusted to 8.0, the suspension was further stirred under the same conditions for 1 h. The solid product was then collected by filtration, rinsed repeatedly with deionized water until the washing solution reached pH 7, and dried at 65 °C overnight. The dried powder was ground and sieved through a 200-mesh screen, and the obtained sample was named SOC. The preparation process is illustrated in Figure 1.

Preparation of SGHC-8

SGOC-8 refers to the GA-cross-linked SOC precursor. SGHC-8 was synthesized by carbonization of SGOC-8 at high temperature. Briefly, 1.0 g of SOC was introduced into 50 mL of acetic acid solution at pH

6.0 and dispersed uniformly. Afterward, 3 mL of GA solution was added, and the suspension was stirred at 500 rpm at 40 °C for 3 h to induce Schiff-base cross-linking between the amino groups of CS and the aldehyde groups of GA. The resulting precursor was collected, rinsed repeatedly with deionized water until the washing solution reached pH 7, and dried at 65 °C overnight. The dried precursor was then carbonized at 1,200 °C for 2 h under flowing N_2 with a ramping rate of 5 °C min^{-1}. After natural cooling, the carbonized product was ground into a uniform powder and named SGHC-8. For comparison, OC was directly carbonized under the same conditions, and the obtained sample was denoted as oxidized coal-derived hard carbon (OHC). The preparation procedure is illustrated in Figure 1. For clarity, SOC refers to the CS-loaded OC precursor without GA treatment, while SGOC-8 denotes the GA-cross-linked CS/OC precursor. After carbonization, the HC obtained from SOC is denoted as chitosan-loaded oxidized coal-derived hard carbon (SHC), and that derived from SGOC-8 is denoted as SGHC-8.

Material characterization

Sample morphology was examined by field-emission scanning electron microscopy (FESEM, JSM-7900F, JEOL Ltd., Japan). X-ray diffraction (XRD) patterns were recorded on a SmartLab SE diffractometer (Rigaku, Japan) using Cu Kα radiation to analyze the crystalline structure. Surface chemical states were analyzed by X-ray photoelectron spectroscopy (XPS) using a Nexsa spectrometer (Thermo Fisher Scientific, USA). Raman measurements were performed using an Explora PLUS Raman microscope (Thermo Fisher Scientific, France) to evaluate the structural disorder of the carbon materials. Fourier transform infrared (FTIR) spectra were recorded using a Nicolet iS20 spectrometer (Thermo Fisher Scientific, USA) to identify functional groups in the precursors, and thermogravimetric analysis (TGA) was performed using a STA449F5 thermogravimetric analyzer (NETZSCH, Germany) to compare their thermal stability. Transmission electron microscopy (TEM) observations and selected-area electron diffraction (SAED) analysis were performed using an FEI Talos F200S microscope (Thermo Fisher Scientific, USA) to investigate the nanostructure and local crystallinity of SGHC-8. The specific surface areas and pore structures of the carbon samples were measured by N_2 adsorption-desorption analysis using a BELSORP-Max analyzer (MicrotracBEL Corp., Japan). Before N_2 adsorption/desorption measurements at 77 K, the samples were degassed at 200 °C for 12 h. Small-angle X-ray scattering (SAXS) measurements were performed using a Xeuss 2.0 SAXS/WAXS system (Xenocs, France) to investigate the internal nanopore structure of the HC samples.

Electrochemical characterization

Electrochemical tests were performed using CR2032-type half cells. To fabricate the working electrodes, active material, acetylene black, and poly(vinylidene fluoride) (PVDF) were blended at a mass ratio of 90:5:5 using N-methyl-2-pyrrolidone (NMP) as the solvent. The obtained slurry was cast onto Cu foil, vacuum-dried at 80 °C overnight, and cut into circular electrodes with a diameter of 16 mm. The final material loading amount on each electrode was approximately 1.0 mg cm^{-2}. The cells were assembled in an Ar-filled glovebox with sodium foil as both the counter and reference electrodes, Whatman GF/D glass fiber as the separator, and 1 mol L^{-1} $NaClO_4$ in ethylene carbonate/dimethyl carbonate (EC/DMC) as the electrolyte. Galvanostatic charge/discharge measurements were conducted on a LAND battery tester within a voltage window of 0.01-3.0 V. Cyclic voltammetry (CV) measurements were performed over 0.01-3.0 V at various scan rates. Electrochemical impedance spectroscopy (EIS) spectra were collected from 100 kHz to 10 mHz. Galvanostatic intermittent titration technique (GITT) was carried out using repeated current-pulse and relaxation steps to analyze Na^+ diffusion behavior. For *ex situ* XRD measurements, the cells were cycled within a voltage window of 0.01-2.5 V, and the electrodes were collected at selected states of discharge and charge for structural characterization.

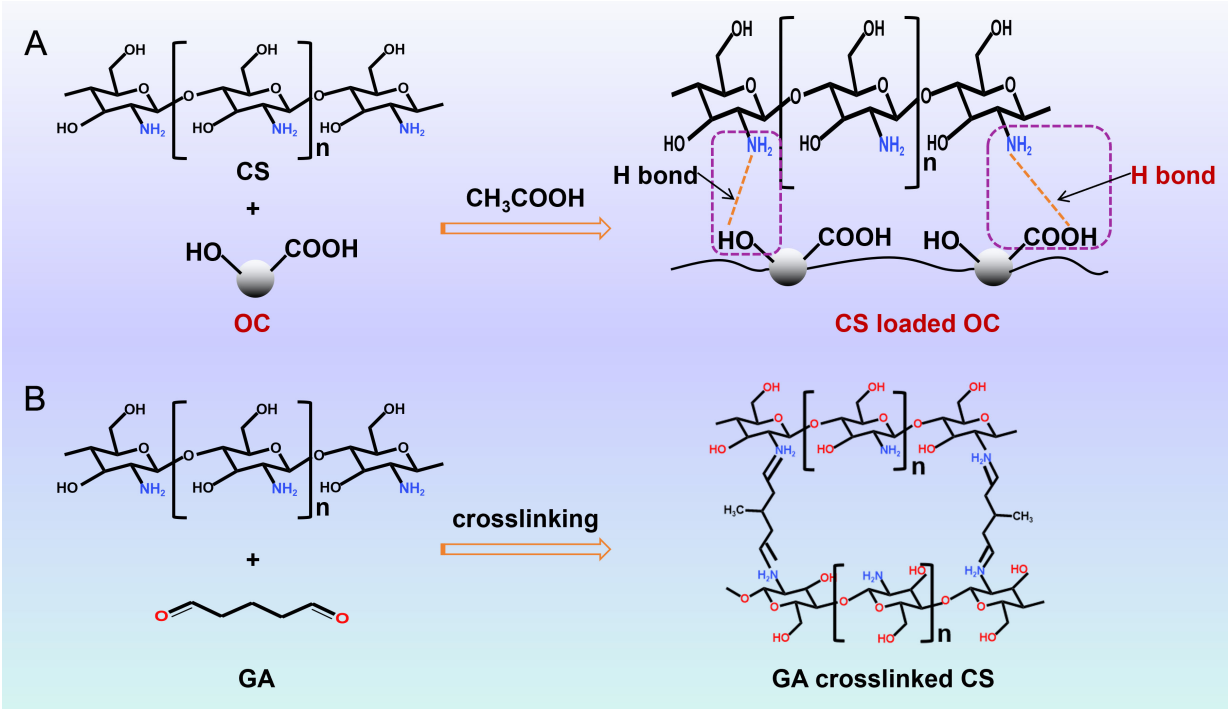

Figure 2. (A) Schematic illustration of CS immobilization on OC, (B) Schiff-base cross-linking reaction between CS and GA. CS: Chitosan; GA: glutaraldehyde; OC: oxidized coal.

RESULTS AND DISCUSSION

Cross-linking design and precursor verification

The synthesis mechanism of cross-linked and nitrogen-doped coal-derived HC is illustrated in Figure 1. The preparation process mainly involves four steps: pre-oxidation of raw coal, CS loading, GA-assisted cross-linking, and high-temperature carbonization. During pre-oxidation, oxygenated functional groups, mainly hydroxyl (-OH) and carboxyl (-COOH) groups, are introduced onto the surface of OC, primarily to provide active sites for subsequent molecular interactions[23]. In acidic aqueous solution, the amino groups (-NH_2) of CS are protonated to form -NH_3^+[24]. The abundant -NH_3^+ groups of CS can interact with the -OH/-COOH groups on OC through hydrogen bonding and electrostatic interactions, enabling CS to be immobilized on the OC surface [Figure 2A].

Subsequently, Schiff-base condensation reaction occurs between the -NH_2 of CS and the aldehyde (-CHO) of GA, generating C=N linkages[25] and a 3D cross-linked network as a precursor for anode material of SIB [Figure 2B]. In this system, CS plays a dual role as both a cross-linking component and an endogenous nitrogen source, enabling the simultaneous construction of a molecular network and in situ nitrogen doping. The obtained cross-linked precursor, denoted as SGOC-8 (m_{CS}/m_{OC} = 8 wt%), can stabilize the coal-derived precursor, restrict carbonization shrinkage, and suppress the ordered growth of graphitic microcrystals during subsequent high-temperature carbonization.

FTIR, XPS, and thermogravimetry (TG) analyses were used to examine the formation of the cross-linked precursor. As shown in Figure 3A, OC exhibits a strong C=O absorption band at 1,710 cm^{-1} and a C-O vibration band at 1,162 cm^{-1} due to the introduction of oxygen-containing functional groups during oxidation. Among the three samples (OC, SOC, and SGOC-8), SGOC-8 displays the strongest -OH/-NH-related absorption, indicating the incorporation of CS. The C=N stretching vibration further evidences Schiff-base condensation between the -NH_2 groups of CS and the -CHO groups of GA. Consistent with the

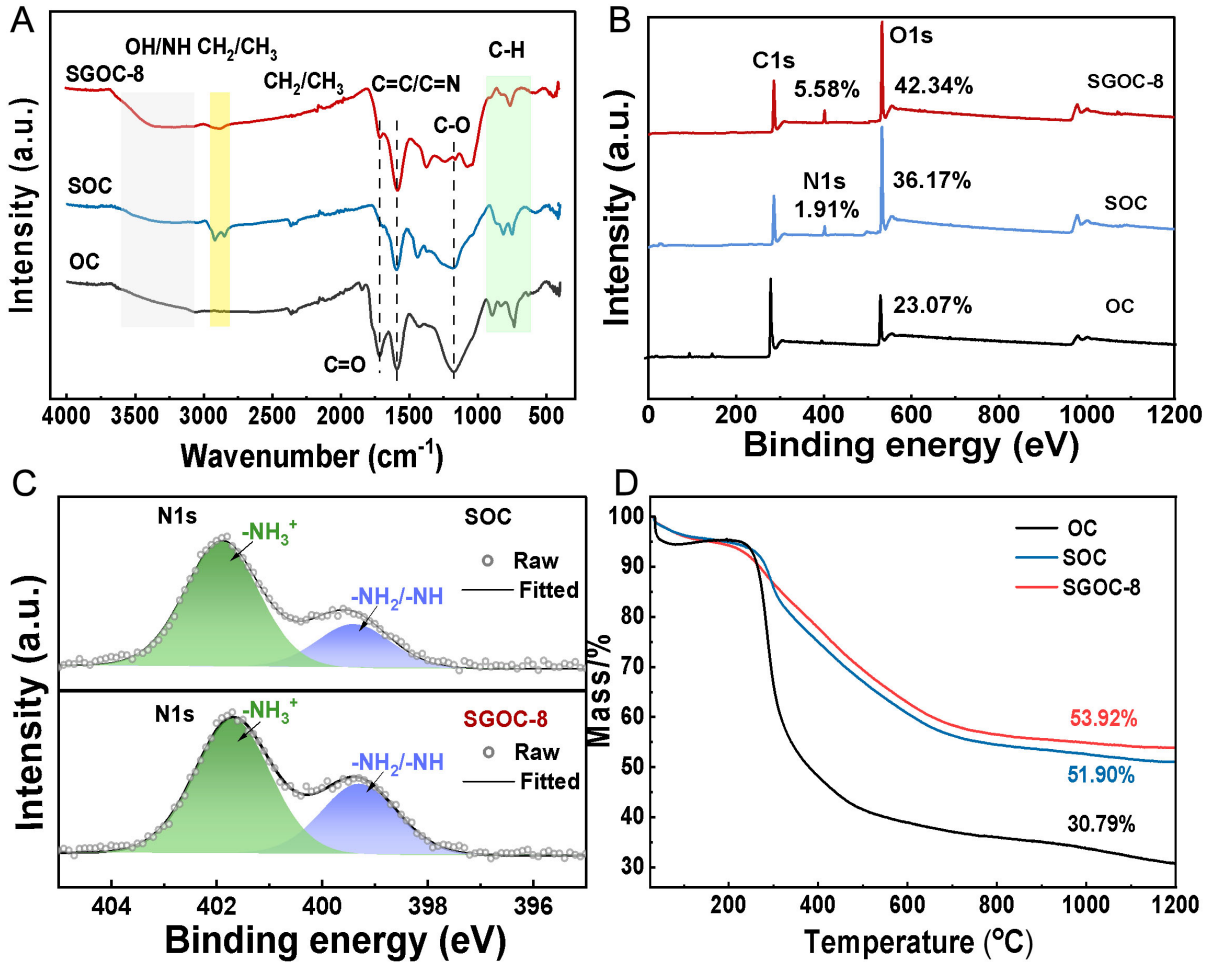

Figure 3. Chemical composition and thermal stability of three samples: (A) FTIR, (B) XPS survey, (C) high-resolution N 1s XPS, and (D) TG curves. FTIR: Fourier transform infrared; XPS: X-ray photoelectron spectroscopy; SOC: chitosan-loaded oxidized coal; TG: thermogravimetry.

FTIR results, the XPS survey spectra in Figure 3B show that SGOC-8 possesses higher O and N contents (42.34% and 5.58%, respectively), further supporting the successful incorporation of CS/GA-derived functionalities. From the fitted high-resolution N 1s spectrum [Figure 3C], two major nitrogen-containing species, -NH_2/-NH and -NH_3^+, are present[26]. The -NH_2/-NH component mainly originates from unreacted amino groups in CS, while the -NH_3^+ constituent is associated with the protonation of amino groups in the acetic acid solution. These results confirm the successful introduction of CS and its interaction with GA. TG curves are further compared to assess the effect of CS/GA crosslinking on the thermal stability of OC. Figure 3D shows that SGOC-8 retains more residual mass than OC and SOC after heating, indicating enhanced thermal stability after CS/GA cross-linking. This enhanced stability suggests that the cross-linked molecular network can stabilize the coal-derived precursor and suppress excessive structural shrinkage during carbonization, which is beneficial for forming expanded interlayers and nanopores in the resulting HC.

Microstructure regulation of SGHC-8

The morphology and microstructure of OHC, SHC, and SGHC-8 were investigated to reveal the effect of cross-linking on carbon structural evolution. As shown in Figure 4A, OHC exhibits a relatively compact polyhedral morphology with well-defined particle edges. In contrast, SHC and SGHC-8 display a smoother and less compact surface morphology [Figure 4B and C]. This morphological change indicates that the

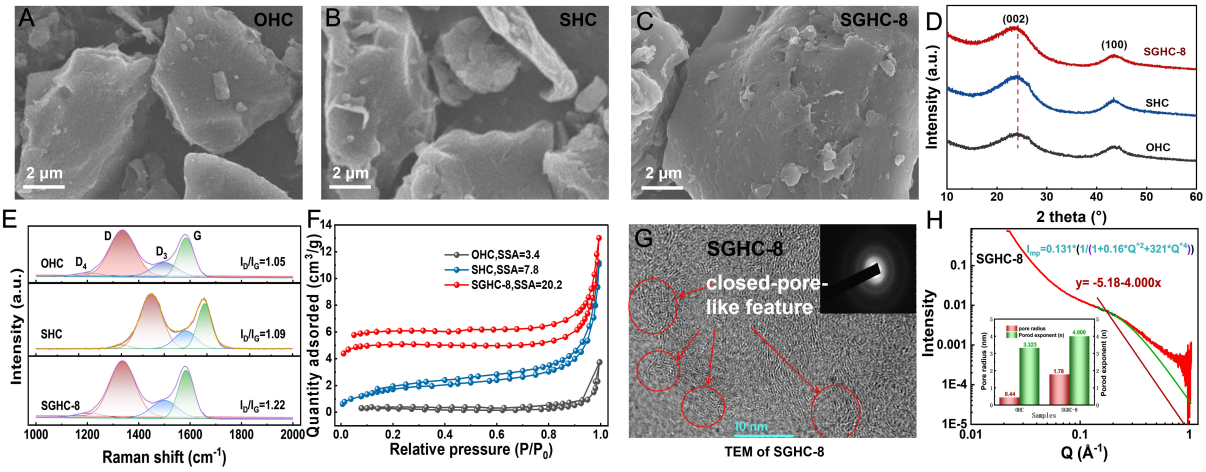

Figure 4. Microstructural characterization of OHC, SHC, and SGHC-8: (A-C) SEM images, (D) XRD patterns, (E) Raman spectra, (F) N_2 adsorption/desorption results, (G) TEM image of SGHC-8, and (H) SAXS profile of SGHC-8 with an inset comparing the characteristic pore radius and Porod exponent of OHC and SGHC-8. XRD: X-ray diffraction; TEM: transmission electron microscopy; SAXS: small-angle X-ray scattering; OHC: oxidized coal-derived hard carbon; SHC: chitosan-loaded oxidized coal-derived hard carbon; SEM: scanning electron microscopy.

CS/GA cross-linked network alters the carbonization behavior of the coal-derived precursor and suppresses the formation of highly ordered carbon domains. The microcrystalline structure of HC plays a decisive role in Na^+ storage behavior[27]. For HC, a layer distance of 0.37-0.40 nm is generally suitable for Na^+ insertion and migration[28]. As shown in Figure 4D, all three samples exhibit two broad XRD reflections corresponding to the (002) and (100) planes of turbostratic carbon. The (002) peak of SHC is close to that of OHC, whereas the (002) peak of SGHC-8 shifts slightly toward a lower angle, indicating enlarged interlayer spacing. The calculated d002 value increases from 0.366 nm for OHC to 0.375 nm for SGHC-8 based on repeated XRD measurements. These results suggest that CS/GA cross-linking can regulate the carbon microcrystalline structure and facilitate the formation of a more disordered carbon framework.

Raman spectra were collected to reflect the number of defects and the degree of disorder of the HC samples. As shown in Figure 4E, the three samples display characteristic D and G bands located at around 1,350 and 1,590 cm^{-1}, which are related to defective/disordered carbon and graphitic sp^2 carbon, respectively[29]. The I_D/I_G ratio increases from 1.05 for OHC, 1.09 for SHC, to 1.22 for SGHC-8, suggesting that CS/GA cross-linking introduces more structural defects. Such enhanced defects may create additional sites for Na^+ adsorption and contribute to the sloping capacity, which agrees well with the XRD analysis. High-resolution C 1s, N 1s, and O 1s XPS spectra were further used to examine the surface chemistry of SGHC-8 [Supplementary Figures 1-3], verifying the retention of nitrogen- and oxygen-containing species after carbonization. N2 adsorption/desorption measurements were used to evaluate the accessible open-pore structure. As shown in Figure 4F, the specific surface areas of OHC, SHC, and SGHC-8 are 3.4, 7.8, and 20.2 $m^2 g^{-1}$, respectively, indicating that the cross-linked precursor facilitates open-pore development. Since internal nanopores are closely related to low-voltage sodium storage[30], TEM and SAXS were further used to investigate the internal pore structure of SGHC-8. As shown in Figure 4G, SGHC-8 exhibits curved carbon layers and closed-pore-like features, suggesting the presence of nanoscale pore structures. SAXS analysis further supports these pore characteristics. Additionally, the scattering vector q was calculated using the following equation for SAXS analysis:

$$q = \frac{4\pi \sin\theta}{\lambda} \quad (1)$$

Here, λ denotes the X-ray wavelength, and θ represents half of the scattering angle. The shoulder feature in the medium-q range originates from internal nanopores in the HC framework. The characteristic pore radius was then estimated using the Guinier equation:

$$I_{(q)} = NV^2 \exp\left(-\frac{R_g^2}{3}q^2\right) \quad (2)$$

$$R = \sqrt{\frac{5}{3}}R_g \quad (3)$$

Where $I_{(q)}$, N, V, R_g, and R denote the scattering intensity, pore number, pore volume, radius of gyration, and pore radius, respectively. SAXS analysis further supports the presence of internal nanopores in SGHC-8 [Figure 4H]. As summarized in the inset, the characteristic pore radius increases from approximately 0.44 nm for OHC to 1.78 nm for SGHC-8, while the corresponding Porod exponent increases from 3.323 to 4.000. These changes further indicate that CS/GA cross-linking substantially alters the internal nanopore structure of the resulting hard carbon.

Based on the chemical composition and microstructural characteristics summarized above, CS/GA cross-linking effectively tailors the morphology, carbon microcrystal structure, defect concentration, and porosity of coal-derived HC. The enlarged interlayer spacing and developed nanopores provide additional Na^+ storage sites and promote low-voltage sodium storage.

Electrochemical sodium-storage performance

SGHC-8, SHC, and OHC were assembled into CR2032 sodium half cells to compare their Na^+ storage properties. The galvanostatic charge/discharge curves are presented in Figure 5A at 0.02 A g^{-1}. All three electrodes show a high-voltage slope and a low-voltage plateau, which are typical features of HC anodes. SGHC-8 achieves the highest reversible capacity of 350.5 mAh g^{-1}, 27.9% higher than that of OHC (274.1 mAh g^{-1}). In addition, SGHC-8 exhibits an initial Coulombic efficiency of 80.6%, slightly exceeding the 78.8% of OHC. Notably, the plateau capacity contribution increases from 45.6% for OHC to 48.5% for SGHC-8. Considering the reversible capacities, the corresponding absolute plateau capacities are approximately 125.0 mAh g^{-1} for OHC (274.1 × 45.6%) and 170.0 mAh g^{-1} for SGHC-8 (350.5 × 48.5%), respectively. This substantial increase in absolute plateau capacity further demonstrates the enhanced low-voltage sodium-storage capability of SGHC-8. The performance of SHC lies between that of OHC and SGHC-8 in terms of both reversible capacity and initial Coulombic efficiency (ICE). Generally, excessive defects and surface functional groups may lead to irreversible electrolyte decomposition and thus compromise ICE[31]. Although SGHC-8 exhibits the highest defect density and specific surface area, it still delivers a slightly higher ICE, suggesting that the CS/GA-cross-linked network enables balanced regulation of defect density, interlayer spacing, and nanopore structure. CV analysis was then carried out to examine the redox behavior of OHC, SHC, and SGHC-8. As shown in Figure 5B and C, all three electrodes exhibit pronounced redox features in the low-potential region. The cathodic response extends into the low-voltage plateau region of 0.01-0.1 V, whereas the corresponding anodic peaks appear at somewhat higher potentials during desodiation. These features are associated with reversible Na^+ insertion/extraction in graphitic microdomains and low-voltage sodium storage in nanovoids. The broad irreversible peaks at ≈1.2 and 0.4 V in the first cycle are associated with initial electrolyte decomposition and SEI formation. Notably, OHC shows more pronounced irreversible reduction signals, indicating more severe interfacial side reactions. In contrast, the weaker irreversible signals of SGHC-8 suggest improved interfacial reversibility, which may be related to the cross-linking-induced internal nanopores that modulate the accessibility of solvated Na^+ and suppress undesirable electrolyte decomposition[32]. In subsequent cycles, the CV curves show good overlap, indicating favorable reversibility of sodium storage.

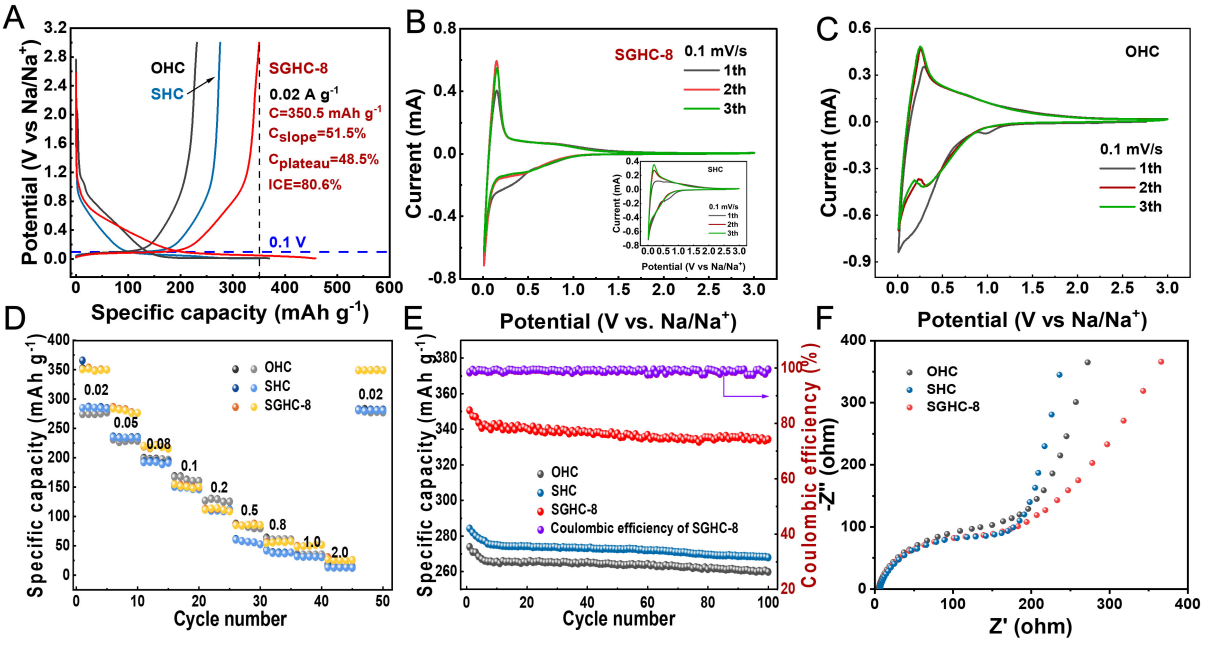

Figure 5. Electrochemical sodium-storage performance: (A) galvanostatic charge/discharge profiles, (B) CV curves of SGHC-8 and SHC, (C) CV curves of OHC, (D) rate performance, (E) cycling performance at 0.02 A g^{-1}, and (F) EIS spectra. EIS: Electrochemical impedance spectroscopy; CV: cyclic voltammetry; OHC: oxidized coal-derived hard carbon; SHC: chitosan-loaded oxidized coal-derived hard carbon.

Rate capability was tested at current densities ranging from 0.02 to 2.0 A g^{-1} [Figure 5D], corresponding approximately to C/17.5 to 5.7 C based on the reversible capacity of SGHC-8. SGHC-8 delivers higher specific capacities than SHC and OHC at 0.02-0.08 A g^{-1}. At 0.1 A g^{-1} and above, however, the capacity differences among the three samples become much smaller, and SGHC-8 no longer shows a clear rate advantage. After the current density returns to 0.02 A g^{-1}, the capacity recovers to 348.9 mAh g^{-1}, indicating that the electrode structure remains stable during repeated sodiation/desodiation. In addition, SGHC-8 preserves 94.8% of its initial reversible capacity after 100 cycles at 0.02 A g^{-1} [Figure 5E], confirming its favorable cycling durability. After the initial activation process, the coulombic efficiency gradually stabilizes and remains close to 100% during subsequent cycling, indicating good reversibility of the sodium-storage process. The different trends between rate capability and cycling performance arise from their different evaluation conditions. The rate capability reflects Na^+ transport kinetics under high current densities, whereas cycling performance mainly depends on structural stability and reversible sodium storage. The improved cycling stability of SGHC-8 is attributed to the stabilized microstructure and abundant sodium-storage sites induced by CS/GA cross-linking.

EIS was further used to compare the interfacial charge-transfer behavior [Figure 5F][33,34]. The three electrodes exhibit comparable Rct values, indicating that the enhanced performance of SGHC-8 does not simply originate from reduced interfacial charge-transfer resistance. Instead, the improved capacity and plateau contribution are mainly associated with CS/GA-induced microstructure regulation, including enlarged interlayer spacing, increased defect density, and abundant nanopores, which provide more accessible sites for Na^+ storage. Moreover, a comparison with previously reported coal-derived HC anodes further underscores the competitive sodium-storage performance of SGHC-8 [Supplementary Table 1].

Sodium-storage kinetics and mechanism of SGHC-8

Rate-dependent CV measurements were first used to analyze the Na^+ storage kinetics of SGHC-8. As shown in Figure 6A, the CV profiles retain similar shapes as the scan rate increases, indicating good electrochemical reversibility. The dependence of peak current on scan rate was fitted using the power-law relationship[35]:

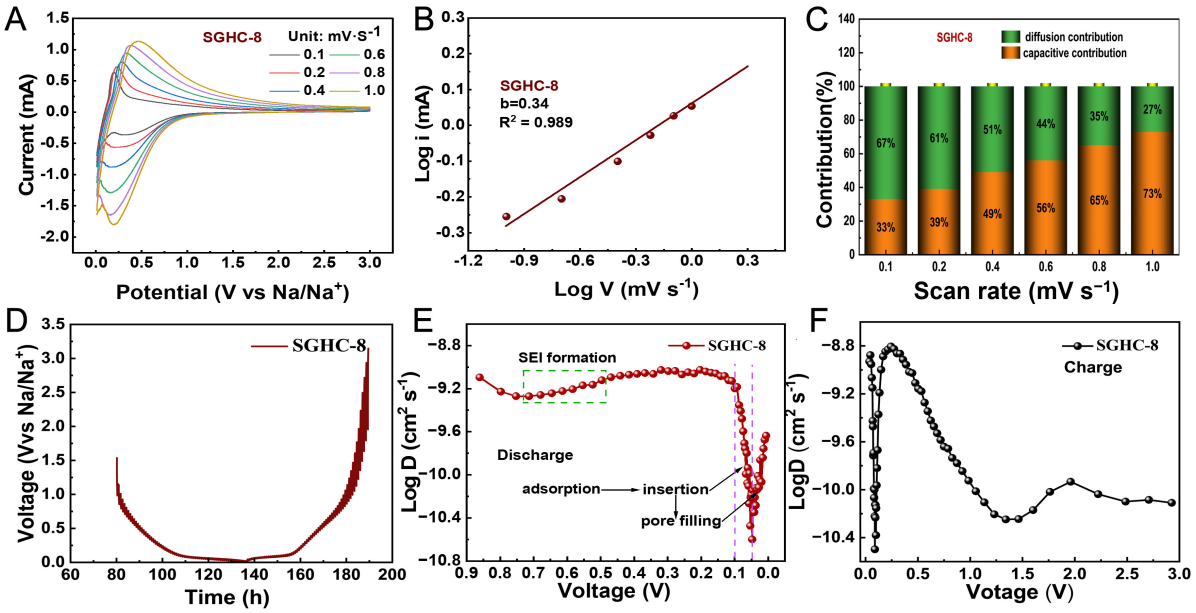

Figure 6. Kinetic analysis of SGHC-8: (A) CV curves at different scan rates, (B) b-value fitting, (C) capacitive and diffusion-controlled contribution ratios, (D) GITT discharge/charge profile, and (E and F) calculated Na^+ diffusion coefficients during discharge and charge. GITT: Galvanostatic intermittent titration technique; CV: cyclic voltammetry.

$$i = av^b \tag{4}$$

where i represents the peak current, v is the scan rate, and a and b are fitting constants. In general, b approaching 0.5 reflects diffusion-dominated kinetics, whereas b close to 1.0 indicates a surface-controlled capacitive response[36]. The fitted b value of SGHC-8 is 0.34 [Figure 6B], indicating pronounced diffusion limitation rather than a surface-controlled capacitive process. This diffusion-dominated feature agrees with the pronounced low-voltage plateau of SGHC-8, which is mainly related to Na^+ intercalation and nanopore filling.

The relative contributions from capacitive and diffusion-controlled processes were further estimated using the following equation[37]:

$$i = k_1 v + k_2 v^{1/2} \tag{5}$$

Here, $k_1 v$ denotes the surface capacitive term, while $k_2 v^{1/2}$ corresponds to the diffusion-controlled term. Figure 6C shows that the diffusion-controlled contribution dominates at low scan rates, corresponding to Na^+ intercalation into expanded interlayers and filling of internal nanopores. As the scan rate increases, the capacitive fraction increases, helping retain rate capability under high-current operation. These results indicate that sodium storage in SGHC-8 involves multiple processes, including surface adsorption, interlayer insertion, and filling of internal nanopores.

GITT was applied to monitor Na^+ transport during sodiation and desodiation [Figure 6D-F]. The derived Na^+ diffusion coefficients exhibit distinct potential-dependent evolution during discharge and charge processes. In the sloping region above 0.1 V, Na^+ diffusion is generally faster than that in the low-voltage plateau region (0.01-0.1 V), suggesting that defect-related adsorption is kinetically more facile, whereas interlayer insertion and nanopore filling in the plateau region involve slower ion transport. The pronounced decrease in Na^+ diffusion coefficient upon entering the low-voltage region is consistent with the transition from surface adsorption to diffusion-controlled interlayer insertion and nanopore filling.

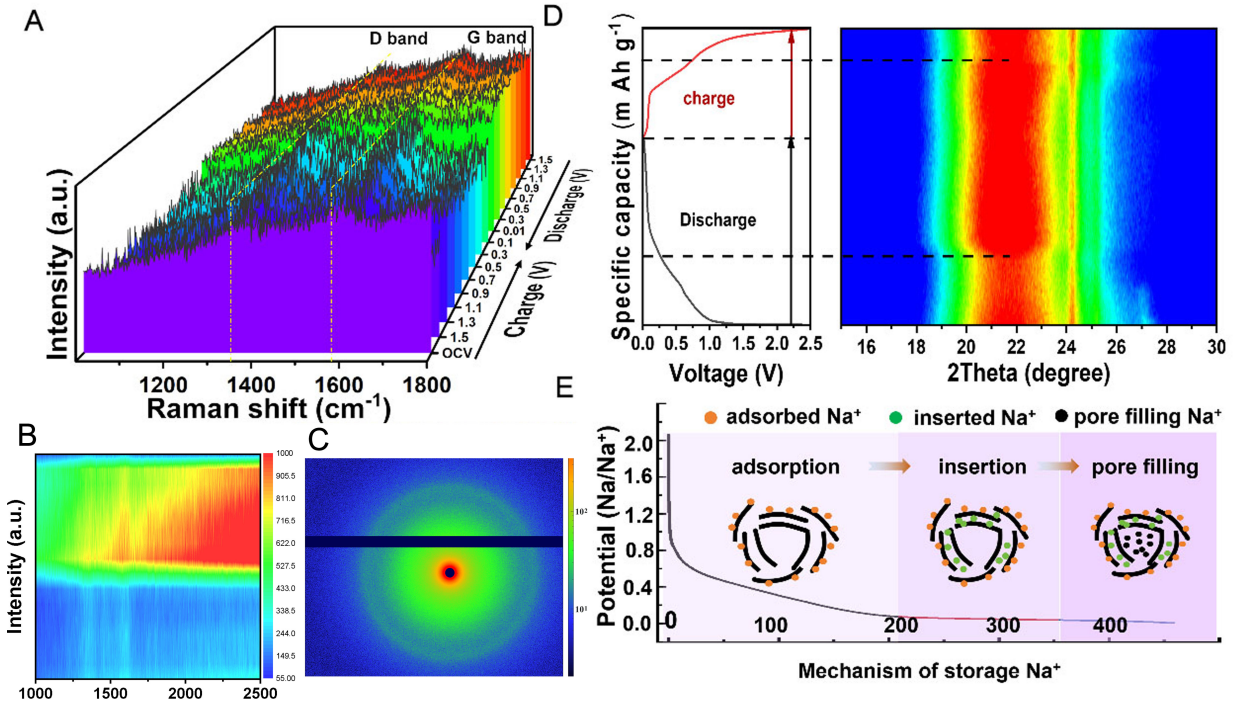

Figure 7. Sodium-storage mechanism of SGHC-8: (A) *ex situ* Raman spectra during discharge/charge, (B) Raman contour map, (C) selected-area electron diffraction (SAED) pattern of SGHC-8, (D) *ex situ* XRD patterns collected during discharge/charge within 0.01-2.5 V, and (E) schematic representation of the proposed Na^+ storage mechanism. XRD: X-ray diffraction.

The low-voltage plateau capacity of HC is generally associated with Na^+ intercalation into graphite-like layers and pore filling within internal nanopores[30]. In some cases, pore filling can further involve the formation of quasi-metallic sodium clusters inside closed pores[38]. In this work, the enlarged interlayer spacing of SGHC-8 is favorable for Na^+ intercalation, while the internal nanopores revealed by TEM and SAXS provide additional sites for low-voltage pore filling. Therefore, the high plateau capacity of SGHC-8 originates from the joint contribution of interlayer intercalation and nanopore filling.

Ex situ Raman and *ex situ* XRD analyses were further used to track the structural evolution of SGHC-8 during sodium storage. As shown in Figure 7A and B, the Raman G band exhibits a reversible shift during discharge and charge, indicating reversible interactions between Na^+ and graphitic nanodomains. The diffuse SAED pattern in Figure 7C further confirms the predominantly disordered nature of SGHC-8, consistent with its turbostratic hard-carbon structure. The *ex situ* XRD patterns in Figure 7D confirm that the interlayer spacing increases during discharge and subsequently recovers upon charge. This behavior supports the contribution of Na^+ intercalation into carbon interlayers in the low-voltage region[39]. In addition, the reversible spectral evolution suggests that the carbon framework maintains structural stability during repeated sodiation/desodiation.

Based on the electrochemical and structural evidence discussed above, sodium storage in SGHC-8 is proposed to follow an adsorption-intercalation-pore-filling process [Figure 7E]. In the high-voltage slope region, Na^+ is preferentially stored at defect sites and accessible pore surfaces. With decreasing potential, Na^+ progressively inserts into expanded graphitic interlayers. In the low-voltage plateau region, internal nanopores are further filled by Na^+, giving rise to the high plateau capacity. Therefore, the improved Na^+ storage performance of SGHC-8 results from the combined regulation of enlarged interlayer spacing, increased defect density, and nanopores enabled by the CS/GA-cross-linked molecular network.

CONCLUSION

In summary, a CS/GA-assisted molecular-network strategy was developed to convert OC into HC with enlarged interlayer spacing and developed nanopores for high-plateau sodium storage. In this design, CS was anchored on OC and then connected by GA to form a three-dimensional network, which restricted the ordered growth of graphitic microcrystals during carbonization. Meanwhile, CS acted as an internal nitrogen source, enabling in situ nitrogen doping and surface-chemistry regulation of the resulting HC. Owing to its enlarged layer spacing, higher defect concentration, and abundant nanopores, SGHC-8 achieved a reversible capacity of 350.5 mAh g^{-1}, an initial Coulombic efficiency of 80.6%, and a plateau capacity contribution of 48.5%. Electrochemical and structural results indicate that sodium storage in SGHC-8 proceeds through an adsorption-intercalation-pore-filling process. This work highlights molecular-network regulation as an effective approach for upgrading coal resources into high-performance HC anodes for SIBs.

DECLARATIONS

Authors' contributions

Conceptualization, funding acquisition, supervision, writing-review and editing: Lu, C.
Investigation, writing-original draft: Dong, Q.
Software, formal analysis: Guo, C.
Methodology: Wang, Z.; Feng, Y.
Data curation, validation: Hu, G.;
Investigation, data curation: Su, T.;
Validation, data curation: Hao, H.
Project administration: Yan, X.
Supervision: Yang, B.
Supervision, writing-review and editing: Cao, D.

Availability of data and materials

The raw data supporting the findings of this study are available within this Article and its Supplementary Materials. Further data are available from the corresponding authors upon request.

AI and AI-assisted tools statement

Not applicable.

Financial support and sponsorship

This work was supported by the Joint Fund of Yulin University and Dalian National Laboratory for Clean Energy (Grant No. YLU-DNL Fund 2025004). Cao, D. acknowledges the financial support from the National Natural Science Foundation of China Regional Innovation and Development Joint Fund (Grant No. U24A2021), the Doctoral Research Startup Fund for High-level Talents at Yulin University (No. 2024GK14), the Industry-University-Research Project of Yulin City Science and Technology Bureau (No. 2025-CXY-139), and the Graduate Innovation and Entrepreneurship Fund Project of Yulin University (No. 2025YLYCX56). Guo, C. also acknowledges Shaanxi Province Natural Science Basic Research Program (Grant No. 2025JC-YBQN-169), Yulin Association for Science and Technology Young Talent Lift Program (Grant No. 20250701), the startup fund for high-level talent Doctoral Research at Yulin University (No. 2023GK66), and Shaanxi Fundamental Science Research Project for Chemistry and Biology (Grant No. 23JHQ090).

Conflicts of interest

All authors declared that there are no conflicts of interest.

Ethical approval and consent to participate

Not applicable.

Consent for publication

Not applicable.

Copyright
© The Author(s) 2026.

Supplementary Materials
Supplementary Materials

REFERENCES

1. Hwang, J. Y.; Myung, S. T.; Sun, Y. K. Sodium-ion batteries: present and future. *Chem. Soc. Rev.* **2017**, *46*, 3529-614. DOI PubMed
2. Chen, T.; Wang, J.; Tan, B.; et al. High-energy, high-power sodium-ion batteries from a layered organic cathode. *J. Am. Chem. Soc.* **2025**, *147*, 6181-92. DOI
3. He, Z.; Huang, Y.; Liu, H.; et al. Anode materials for fast charging sodium-ion batteries. *Nano. Energy.* **2024**, *129*, 109996. DOI
4. Bai, J.; Li, Z.; Wang, X.; Świerczek, K.; Wu, C.; Zhao, H. Limitations and strategies toward high-performance red phosphorus materials for Li/Na-ion batteries. *Energy. Mater. Adv.* **2024**, *5*, 0086. DOI
5. Chu, Y.; Zhang, J.; Zhang, Y.; et al. Reconfiguring hard carbons with emerging sodium-ion batteries: a perspective. *Adv. Mater.* **2023**, *35*, e2212186. DOI
6. Xue, Z.; Yang, S.; Zhang, S.; et al. Review on the application of nanocarbon materials for lithium and sodium metal batteries. *Energy. Mater. Adv.* **2025**, *6*, 0415. DOI
7. Zhao, Y.; Zhang, R.; Hao, J.; et al. Understanding the carbonization-controlled microstructure regulation in coal-based hard carbon to strengthen sodium storage performance. *Phys. Chem. Chem. Phys.* **2025**, *27*, 11752-61. DOI
8. He, X. X.; Li, L.; Wu, X.; Chou, S. L. Sustainable hard carbon for sodium-ion batteries: precursor design and scalable production roadmaps. *Adv. Mater.* **2025**, *37*, e2506066. DOI
9. Wang, X.; Zhang, K.; Su, M.; et al. Coal-derived flaky hard carbon with fast Na^+ transport kinetic as advanced anode material for sodium-ion batteries. *Carbon* **2024**, *229*, 119526. DOI
10. Zhao, G.; Xu, T.; Zhao, Y.; et al. Conversion of aliphatic structure-rich coal maceral into high-capacity hard carbons for sodium-ion batteries. *Energy. Storage. Mater.* **2024**, *67*, 103282. DOI
11. Wang, Y.; Li, M.; Zhang, Y.; Zhang, N. Hard carbon for sodium storage: mechanism and performance optimization. *Nano. Res.* **2024**, *17*, 6038-57. DOI
12. Lu, H.; Sun, S.; Xiao, L.; et al. High-capacity hard carbon pyrolyzed from subbituminous coal as anode for sodium-ion batteries. *ACS. Appl. Energy. Mater.* **2019**, *2*, 729-35. DOI
13. Zhang, W.; Song, R.; Meng, H.; et al. Manipulating surface chemistry on the microarchitecture of coal-based hard carbon for improved sodium storage. *Adv. Sci.* **2025**, *12*, e13835. DOI
14. Chen, H.; Sun, N.; Zhu, Q.; Soomro, R. A.; Xu, B. Microcrystalline hybridization enhanced coal-based carbon anode for advanced sodium-ion batteries. *Adv. Sci.* **2022**, *9*, e2200023. DOI PubMed PMC
15. Zhao, X.; Shi, P.; Wang, H.; et al. Unlocking plateau capacity with versatile precursor crosslinking for carbon anodes in Na-ion batteries. *Energy. Storage. Mater.* **2024**, *70*, 103543. DOI
16. Chen, H.; Sun, N.; Wang, Y.; Soomro, R. A.; Xu, B. One stone two birds: pitch assisted microcrystalline regulation and defect engineering in coal-based carbon anodes for sodium-ion batteries. *Energy. Storage. Mater.* **2023**, *56*, 532-41. DOI
17. Barbosa, R. F. S.; Shyam, S.; Misra, S.; Mitra, S. K.; Rosa, D. S. Chitosan hydrogels crosslinked with glutaraldehyde for potential toxic elements removal: batch and purification device analysis. *J. Appl. Polymer. Sci.* **2025**, *142*, e57539. DOI
18. Agrawal, A.; Janakiraman, S.; Biswas, K.; Venimadhav, A.; Srivastava, S.; Ghosh, S. Understanding the improved electrochemical performance of nitrogen-doped hard carbons as an anode for sodium ion battery. *Electrochim. Acta.* **2019**, *317*, 164-72. DOI
19. Shafiee, F. N.; Mohd Noor, S. A.; Mohd Abdah, M. A. A.; Jamal, S. H.; Samsuri, A. Recent progress on hard carbon and other anode materials for sodium-ion batteries. *Heliyon* **2024**, *10*, e29512. DOI PubMed PMC
20. Huang, J.; Liu, L.; Fan, Q.; Li, S.; Cui, H.; Xu, J. Nitrogen-doped hard carbon anode from redwood biomass for sodium-ion batteries with high initial coulombic efficiency and enhanced rate capability. *Small* **2025**, *21*, e2505579. DOI
21. Zhang, T.; Zhang, T.; Wang, F.; Ran, F. High-efficiently doping nitrogen in kapok fiber-derived hard carbon used as anode materials for boosting rate performance of sodium-ion batteries. *J. Energy. Chem.* **2024**, *96*, 472-82. DOI
22. Wang, K.; Sun, F.; Wang, H.; et al. Altering thermal transformation pathway to create closed pores in coal-derived hard carbon and boosting of Na^+ plateau storage for high-performance sodium-ion battery and sodium-ion capacitor. *Adv. Funct. Mater.* **2022**, *32*, 2203725. DOI

23. Yang, Z.; Zhang, Y.; Zhou, H.; et al. Partial oxidation strategy toward carbonyl-dominated surfaces for enhanced sodium storage in biomass-derived hard carbon. *Carbon. Neutral.* **2025**, *4*, e70057. DOI
24. Sorlier, P.; Denuzière, A.; Viton, C.; Domard, A. Relation between the degree of acetylation and the electrostatic properties of chitin and chitosan. *Biomacromolecules* **2001**, *2*, 765-72. DOI PubMed
25. Schiffman, J. D.; Schauer, C. L. Cross-linking chitosan nanofibers. *Biomacromolecules* **2007**, *8*, 594-601. DOI PubMed
26. Khorsandi, Z.; Borjian-boroujeni, M.; Yekani, R.; Varma, R. S. Carbon nanomaterials with chitosan: a winning combination for drug delivery systems. *J. Drug. Deliv. Sci. Technol.* **2021**, *66*, 102847. DOI
27. Chen, Q.; Yang, Z.; Zhao, P.; et al. Thermal gradients optimizing the microstructure of hard carbon for practical sodium-ion batteries. *Carbon. Neutral.* **2026**, *5*, e70112. DOI
28. Chen, X.; Liu, C.; Fang, Y.; et al. Understanding of the sodium storage mechanism in hard carbon anodes. *Carbon. Energy.* **2022**, *4*, 1133-50. DOI
29. Zhao, J.; He, X.; Lai, W.; et al. Catalytic defect-repairing using manganese ions for hard carbon anode with high-capacity and high-initial-coulombic-efficiency in sodium-ion batteries. *Adv. Energy. Mater.* **2023**, *13*, 2300444. DOI
30. Guo, Y.; Ji, S.; Liu, F.; et al. A review of the preparation and characterization techniques for closed pores in hard carbon and their functions in sodium-ion batteries. *Energy. Mater.* **2025**, *5*, 500030. DOI
31. Li, N.; Yang, Q.; Wei, Y.; et al. Phosphorus-doped hard carbon with controlled active groups and microstructure for high-performance sodium-ion batteries. *J. Mater. Chem. A.* **2020**, *8*, 20486-92. DOI
32. Zhang, Y.; Zhang, S. W.; Chu, Y.; et al. Redefining closed pores in carbons by solvation structures for enhanced sodium storage. *Nat. Commun.* **2025**, *16*, 3634. DOI PubMed PMC
33. Li, Y.; Hu, Y.; Qi, X.; et al. Advanced sodium-ion batteries using superior low cost pyrolyzed anthracite anode: towards practical applications. *Energy. Storage. Mater.* **2016**, *5*, 191-7. DOI
34. Huang, G.; Kong, Q.; Yao, W.; Wang, Q. High proportion of active nitrogen-doped hard carbon based on mannich reaction as anode material for high-performance sodium-ion batteries. *ChemSusChem* **2023**, *16*, e202202070. DOI PubMed
35. Guo, Z.; Xu, Z.; Xie, F.; et al. Investigating the superior performance of hard carbon anodes in sodium-ion compared with lithium- and potassium-ion batteries. *Adv. Mater.* **2023**, *35*, e2304091. DOI
36. Rao, Y. B.; Sundman, O.; Holmboe, M.; Tavajohi, N.; Ohlin, C. A. Scotch pine cones-derived hard carbon as an anode material for sodium-ion battery applications. *ACS. Omega.* **2025**, *10*, 11158-67. DOI PubMed PMC
37. Su, M.; Zhang, K.; Ang, E. H.; et al. Structural regulation of coal-derived hard carbon anode for sodium-ion batteries via pre-oxidation. *Rare. Metals.* **2024**, *43*, 2585-96. DOI
38. None Nagmani, S.; Puravankara, S. Hierarchically porous closed-pore hard carbon as a plateau-dominated high-performance anode for sodium-ion batteries. *Chem. Commun.* **2024**, *60*, 3071-4. DOI PubMed
39. Komaba, S.; Murata, W.; Ishikawa, T.; et al. Electrochemical Na insertion and solid electrolyte interphase for hard-carbon electrodes and application to Na-ion batteries. *Adv. Funct. Mater.* **2011**, *21*, 3859-67. DOI

Disclaimer/Publisher's Note: All statements, opinions, and data contained in this publication are solely those of the individual author(s) and contributor(s) and do not necessarily reflect those of OAE and/or the editor(s). OAE and/or the editor(s) disclaim any responsibility for harm to persons or property resulting from the use of any ideas, methods, instructions, or products mentioned in the content.

© The Author(s) 2026. Open Access This article is licensed under a Creative Commons Attribution 4.0 International License (https://creativecommons.org/licenses/by/4.0/), which permits unrestricted use, sharing, adaptation, distribution and reproduction in any medium or format, for any purpose, even commercially, as long as you give appropriate credit to the original author(s) and the source, provide a link to the Creative Commons license, and indicate if changes were made.